

Colliding stellar wind modelling of the X-ray emission from WR 140

Svetozar A. Zhekov^{*}

*Institute of Astronomy and National Astronomical Observatory (Bulgarian Academy of Sciences),
72 Tsarigradsko Chaussee Blvd., Sofia 1784, Bulgaria*

ABSTRACT

We modelled the *Chandra* and *RXTE* X-ray spectra of the massive binary WR 140 in the framework of the *standard* colliding stellar wind (CSW) picture. Models with partial electron heating at the shock fronts are a better representation of the X-ray data than those with complete temperature equalization. Emission measure of the X-ray plasma in the CSW region exhibits a considerable decrease at orbital phases near periastron. This is equivalent to variable effective mass-loss rates over the binary orbit. At orbital phases near periastron, a considerable X-ray absorption in *excess* to that from the stellar winds in WR 140 is present. The *standard* CSW model provides line profiles that in general do *not* match well the observed line profiles of the strong line features in the X-ray spectrum of WR 140. The variable effective mass-loss rate could be understood *qualitatively* in CSW picture of clumpy stellar winds where clumps are efficiently dissolved in the CSW region near apastron but not at periastron. However, future development of CSW models with *non-spherically-symmetric* stellar winds might be needed to get a better correspondence between theory and observations.

Key words: shock waves — stars: individual: WR 140 — stars: Wolf-Rayet — X-rays: stars.

1 INTRODUCTION

Massive stars of early spectral types, Wolf-Rayet (WR) and OB, possess massive and fast supersonic stellar winds ($V_{wind} = 1000 - 5000 \text{ km s}^{-1}$; $\dot{M} \sim 10^{-7} - 10^{-4} M_{\odot} \text{ yr}^{-1}$). If a binary consists of two massive stars, the interaction of their supersonic winds will result in enhanced X-ray emission of such an object, originating from plasma heated in colliding-stellar-wind (CSW) shocks, as first proposed by Cherepashchuk (1976) and Prilutskii & Usov (1976). Due to the high velocities of stellar winds in massive stars, X-rays from such binaries provide direct pieces of information about the shocked plasma. Thus, the wind collision in a massive binary could simply serve as an excellent laboratory to test our understanding of physical processes in extreme conditions of strong shocks: high temperatures, rarefied plasmas etc. To do so, we need to confront our CSW theories with good experimental data, that is with X-ray observations of very good quality that provide spectra with considerable detail (e.g., with high spectral resolution, orbital coverage).

Although the first systematic X-ray survey of WRs with the *Einstein* Observatory showed that WR+O binaries are the brightest X-ray sources amongst them (Pollock 1987), only the modern X-ray observatories launched in the last two decades or so provided such high-quality data sets that would allow us to carry out the corresponding theoretical CSW studies in great detail (see Rauw & Nazé 2016 for a review on the progress of studies of X-ray emission from interacting wind massive binaries of early spectral types).

It is worth noting that for efficient testing of our theories, we need not only X-ray data with good quality, but we need the binary and stellar parameters of this studied object to be well constrained as

well. From such a point of view, WR 140 is probably the ‘best’ object amongst the massive WR binaries. So, the goal of the current study of the colliding stellar wind phenomenon is to carry out a direct comparison of the CSW model results and high-quality X-ray observations of the massive Wolf-Rayet binary WR 140: a long-time pending study. We note that a direct confrontation of CSW models and observations of WR 140 has been carried out but only for four low-resolution (undispersed) *ASCA* spectra (Zhekov & Skinner 2000).

Our paper is organized as follows. In Section 2, we provide some basic parameters of WR 140 adopted in this study. In Section 3, we describe the archival X-ray observations of WR 140. In Section 4, we give details about the CSW modelling of the X-ray spectra of WR 140 and the corresponding results. In Section 5, we discuss our results, and we present our conclusions in Section 6.

2 THE WOLF-RAYET BINARY WR 140

The WR star WR 140 (HD 193793) is a massive binary (WC7pd+O4-5¹) that is fairly considered the prototype of colliding wind binaries. It shows variable X-ray, radio and infrared emission over its ~ 7.9 -year orbital period (Williams et al. 1990). WR 140 is also one of the seven WR binaries which originally defined the group of the so-called periodic dust makers (Williams 1995, Williams 2008 and references therein).

Its orbital parameters are well constrained as a result from extensive studies in the optical and near-infrared spectral domains (e.g.,

¹ Galactic Wolf Rayet Catalogue; <http://pacrowther.staff.shef.ac.uk/WRcat/index.php>

^{*} E-mail: szhekov@astro.bas.bg

Table 1. WR 140 parameters adopted in this work for use in the CSW model

Parameter	Value	Reference
T_0 (MJD)	46154.8	(1)
Period (days)	2896.35	(1)
ω (deg)	46.8	(1)
Inclination (deg)	119.6 (60.4)	(1)
Eccentricity	0.8964	(1)
Semi-major axis (au)	14.73	(1)
V_{WR} (km s ⁻¹)	2860	(2)
\dot{M}_{WR} (M _⊙ yr ⁻¹)	4.04×10^{-5}	(2)
V_O (km s ⁻¹)	3200	(2)
\dot{M}_O (M _⊙ yr ⁻¹)	1.275×10^{-6}	(2)
Distance (pc)	1641	(4)

Note. (1) Orbital parameters are from [Monnier et al. \(2011\)](#) (see table 2 therein). (2) [Williams et al. \(1990\)](#) as the mass-loss rates were re-scaled to the *Gaia* distance. (3) The *Gaia* distance from ([Bailer-Jones et al. 2018](#)) and ([Rate & Crowther 2020](#)).

[Marchenko et al. 2003](#), [Fahed et al. 2011](#), [Monnier et al. 2011](#)). For this study, we use the orbital parameters of WR 140 inclination angle (i), eccentricity (e), semi-major axis from [Monnier et al. \(2011\)](#) and we note that the adopted distance by these authors (1670 pc) differs by less than 2% from the *Gaia* distance of $d = 1641^{+81}_{-74}$ pc ([Bailer-Jones et al. 2018](#)) and $d = 1640^{+110}_{-90}$ pc ([Rate & Crowther 2020](#)) to this object.

For the stellar wind parameters (velocity and mass loss; V_{WR} , \dot{M}_{WR} , V_O , \dot{M}_O), we adopt the corresponding values from [Williams et al. \(1990\)](#) as the mass-loss rates were re-scaled to the *Gaia* distance and adopting a modest volume filling factor of 0.25. Table 1 summarises the WR 140 parameters adopted in this study.

Based on the [Monnier et al. \(2011\)](#) ephemeris, we derive that the WR star is in front at orbital phase = 0.00319, while the O star is in front at orbital phase = 0.95516.

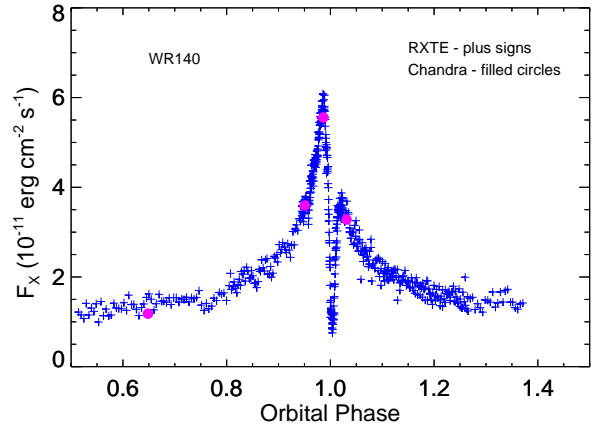
3 OBSERVATIONS AND DATA REDUCTION

In this study we made use of archive X-ray data from observations with the *Chandra* and *RXTE* (Rossi X-ray Timing Explorer) X-ray observatories. These data sets provide a very dense coverage of the orbital period of WR 140 (*RXTE*) and high-resolution X-ray spectra with good photon statistics (*Chandra*).

3.1 Observations with *Chandra*

We used seven observations with the *Chandra* High-Energy Transmission Gratings (HETG) carried out in the period 2000 December - 2008 August: Obs ID 2337, 2338, 5419, 6286, 6287, 8911 and 9909. Following the Science Threads for Grating Spectroscopy in the CIAO 4.12² data analysis software, we extracted the WR 140 X-ray spectra from these data sets (we have initially re-processed the data adopting the CIAO CHANDRA_REPRO script). In this study, we used the first-order Medium Energy Grating (MEG) and High Energy Grating (HEG) spectra. We constructed a total spectrum for observations with orbital phases that are very close and no spectral change is expected. Thus, we end up with four data sets Obs 1 (2337),

² Chandra Interactive Analysis of Observations (CIAO), <https://cxc.harvard.edu/ciao/>.

**Figure 1.** The observed X-ray flux in the (3 - 10 keV) energy range from the *Chandra* and *RXTE* observations of WR 140.

Obs 2 (2338), Obs 3 (5419, 6286, 6287) and Obs 4 (8911, 9909) that provide high-quality spectra with good spectral resolution. The total number of source counts in the corresponding MEG and HEG spectra are 50009, 26064 (Obs 1); 5150, 3833 (Obs 2); 54648, 24854 (Obs 3); 71273, 32324 (Obs 4). The *Chandra* calibration database CALDB v.4.9.0 was used to construct the response matrices and the ancillary response files.

A conventional X-ray analysis (i.e., using discrete-temperature plasma models, deriving line profile parameters etc.) of some of these data was presented in [Pollock et al. \(2005\)](#).

3.2 Observations with *RXTE*

We used 552 archive *RXTE* spectra of WR 140. The observations were carried out in the period 2000 December - 2011 December being part of eight observational programmes P60004, P70003, P91002, P92003, P93001, P94001, P95303 and P96300. The typical exposure times were of 500 - 2200 s that resulted in good to excellent (700 - 50000 source counts) undispersed X-ray spectra at energies above 2-3 keV. For the spectral analysis, we used all the source and background spectra, and response files as provided in the *RXTE* archive³.

Some of these data (P60004) were presented and discussed in [Pollock et al. \(2005\)](#) and [Russell et al. \(2011\)](#), while results from spectral analysis of the entire *RXTE* data set are shown in fig. 2 in [Pollock \(2012\)](#).

Anticipating the results from the CSW modelling of the X-ray spectra of WR 140, the observed X-ray flux is shown in Fig. 1. We see that there is a good correspondence between the observed flux values from *RXTE* and *Chandra* observations for similar orbital phases. This gives us confidence that both spectral data set can be used to test in detail the CSW picture in this massive binary system.

For the spectral analysis in this study, we made use of standard as well as custom models in version 12.10.1 of XSPEC ([Arnaud 1996](#)).

³ We used *RXTE* data provided by the High Energy Astrophysics Science Archive Research Center (HEASARC), <https://heasarc.gsfc.nasa.gov/>.

4 SPECTRAL MODELLING

4.1 CSW model

The standard physical picture of CSWs in massive binaries considers interaction of two spherically-symmetric stellar winds, which have reached their terminal velocities in front of the shocks. The interaction region has cylindrical symmetry and two-dimensional (2D) numerical hydrodynamic models could be used for calculating the physical parameters of the CSW structure. Figure 2 shows a schematic diagram of the wind interaction of two spherically-symmetric stellar winds in a WR+O binary. We note that here, as in our previous works, we adopt a convention that the O star in the binary system is located at the origin of the coordinate system.

As shown in the early works by Lebedev & Myasnikov (1990), Luo et al. (1990), Stevens et al. (1992) and Myasnikov & Zhekov (1993), the basic input parameters for the CSW hydrodynamic model in WR+O binaries are the mass loss and velocity of the stellar winds of the binary components and the binary separation. Following the parameter notation from Myasnikov & Zhekov (1993), we note that the shape and the structure of the CSW interaction region are defined by a dimensionless parameter $\Lambda = (\dot{M}_{WR}V_{WR})/(\dot{M}_O V_O)$ representing the ram-pressure ratio of the stellar winds of the binary components.

It is important to note that various mechanisms may play an important role for the physics of the CSW region. For example, CSW shocks could be adiabatic or radiative, partial electron heating might occur behind strong shocks, non-equilibrium ionization (NEI) effects could affect the X-ray emission from the CSW region. The importance of each physical mechanism could be estimated based on some dimensionless parameters: (a) parameters χ (see eq. 8 in Stevens et al. 1992) and Γ_{ff} (see eq.9 in Myasnikov & Zhekov 1993) show whether or not the shock plasma is adiabatic; (b) parameter Γ_{eq} (see eq. 1 in Zhekov & Skinner 2000) determines whether the difference of electron and ion temperatures is important; (c) parameter Γ_{NEI} (see eq. 1 in Zhekov 2007) estimates the significance of the NEI effects.

Based on the nominal values of the stellar wind parameters and binary separation (Section 2), Figure 3 shows the corresponding values of these dimensionless parameters for the entire orbit of WR 140 (i.e., the range of binary separation 0.1036–1.8964 in units of semi-major axis). We see that CSW models that consider adiabatic shocks are suitable for the case of WR 140. The shock-heated plasma should have different electron and ion temperatures ($T_e \neq T_i$). And, the NEI effects are not important that is the X-ray emission originates from plasma in collisional ionization equilibrium (CIE).

For modelling all X-ray spectra of WR 140 in this study, these estimates justify the use of our CSW *xSPEC* model that takes into account the different electron and ion temperature behind the shocks. All details of the model are found in Zhekov & Skinner (2000) but we nevertheless list the basic physical features of the model. Namely, along the entire shock surfaces of the CSW region the ratio of the local post-shock *electron* temperature to the mean post-shock plasma temperature is defined by a single parameter (β). The evolution of the electron temperature is followed along each streamline behind the shock surfaces. No thermal broadening is considered. The latter has no effect for undispersed X-ray spectra but might have some effect for high-resolution grating spectra. However, anticipating some basic results from the current analysis (see Section 4.2; Figs. 8, 9, we are confident to assume that considering the effects of thermal broadening could be left beyond the scope of this study.

For modelling the X-ray spectra with high spectral resolution, we used the *xSPEC* model that explicitly takes into account the

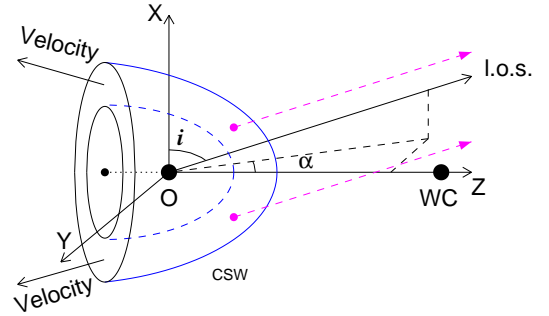


Figure 2. Schematic diagram of colliding stellar winds in a massive WC+O binary system (e.g., WR 140). The wind interaction ‘cone’ is denoted by CSW (the axis Z is its axis of symmetry; the axis X is perpendicular to the orbital plane; the axis Y completes the right-handed coordinate system). The line-of-sight towards observer is denoted by l.o.s. and the two related angles, i (orbital inclination) and α (azimuthal angle) are marked as well. The arrows labelled ‘Velocity’ indicate the general direction of the bulk gas velocity in the interaction region. The two dashed-line arrows (in magenta colour) illustrate that emission from a parcel of gas in the CSW region may experience different wind absorption (passing closer or further from one or both stars in the binary): this depends on the azimuthal angle and rotational angle around the axis of symmetry (Z).

line broadening (bulk gas velocities) from the hydrodynamic CSW model (Zhekov & Park 2010). A new feature was also added in this *xSPEC* model, namely, it now considers the specific stellar wind (WR and/or O-star) absorption along the line of sight to the observer for each parcel of gas in the CSW region. This is done in a ‘cold’-wind approximation.

It is important to note that our *xSPEC* models can take into account the different chemical composition of the WR and O-star wind in modelling the X-ray emission from the CSW region in WR 140. This is because they are based on the 2D numerical hydrodynamic model of CSW by Lebedev & Myasnikov (1990) (see also Myasnikov & Zhekov 1993), which provides an exact solution to all discontinuity surfaces (the two shocks and the contact discontinuity) of the CSW region. This means that the X-ray emission from the shocked WR and O-wind plasma can be modelled separately.

Finally, for clarity we provide the details of our fitting procedure as given in section 4.1 of Zhekov (2017). “Our entire fitting procedure is threefold: (a) given the stellar wind and binary parameters, the hydrodynamic model provides the physical parameters of the CSW region; (b) based on these results, we prepare the input quantities (e.g., distribution of temperature, emission measure, ionization age, bulk gas velocity) for the *spectral* model in *xSPEC*; (c) the CSW *xSPEC* model fits the observed X-ray spectrum. Note that in *xSPEC* we can fit for the X-ray absorption, chemical abundances and the model normalization parameter. If adjustments of other physical parameters are required, all three steps should be repeated: i.e., our fitting procedure is an iterative process. It is important to keep in mind that the normalization parameter (*norm*) of the CSW model in *xSPEC* is a dimensionless quantity that gives the ratio of observed to theoretical fluxes. Thus, the entire fitting procedure is aimed at getting a value of $norm = 1.0$, which indicates a perfect match between the observed count rate and that predicted by the model ($norm < 1.0$ indicates a

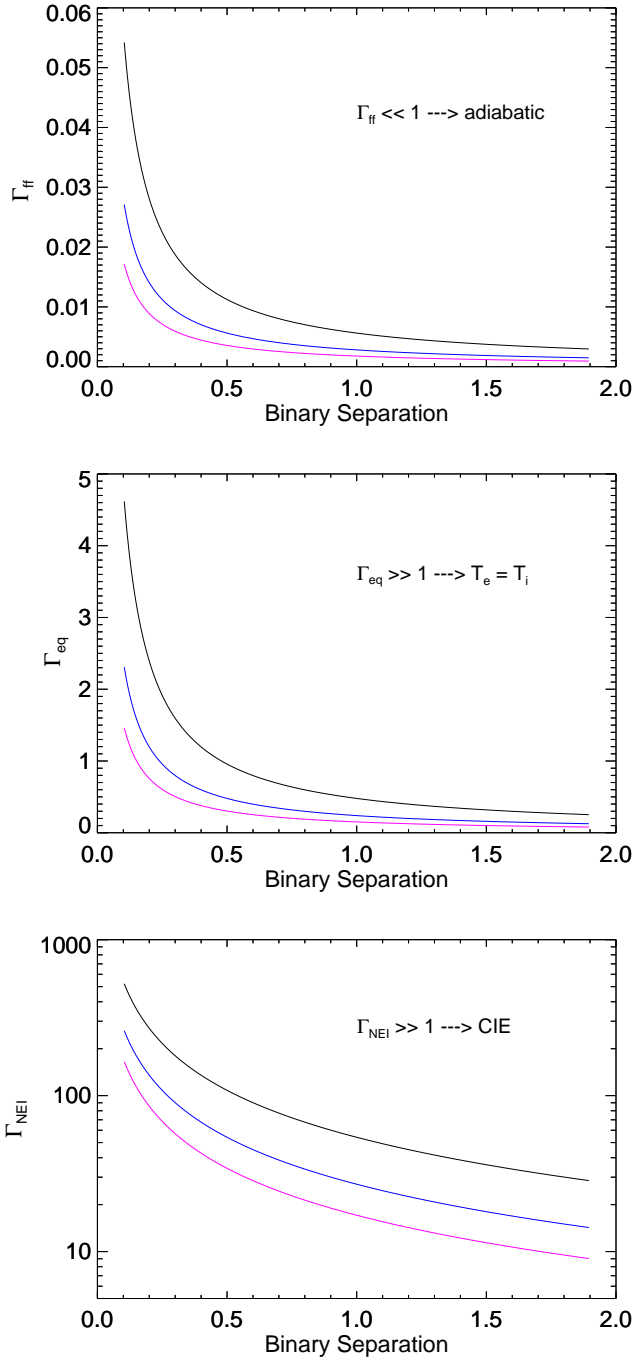


Figure 3. The dependence of dimensionless CSW parameters Γ_{ff} , Γ_{eq} and Γ_{NEI} on the range of binary separation over the entire orbit of WR 140. For comparison, the cases with reduced mass-loss rates of 0.25 and 0.1 their nominal values are shown in blue and magenta colour, respectively. Binary separation is in units of the semi-major axis.

theoretical flux higher than that required by the observations and the opposite is valid for $norm > 1.0$."

Since we are dealing with X-ray emission from thermal plasma, $norm = 1$ (or $norm < 1.0$; $norm > 1.0$) shows whether the theoretical model predicts an amount of emission measure exactly as needed (or higher/smaller than that) to explain the observed X-ray emission.

Table 2. WR 140 Spectral Fit Results (abundances)

	C / He = 0.1	C / He = 0.4
Ne	0.75 ± 0.02	1.10 ± 0.06
Mg	0.29 ± 0.03	0.44 ± 0.03
Si	0.93 ± 0.04	1.37 ± 0.07
S	1.67 ± 0.08	2.43 ± 0.11
Ar	1.91 ± 0.11	2.50 ± 0.35
Ca	0.52 ± 0.35	0.55 ± 0.51
Fe	1.14 ± 0.05	1.61 ± 0.15

Note. Abundance values derived from the simultaneous fits to the *Chandra*-MEG spectra by making use of the CSW model that takes into account different electron and ion temperatures: $\beta = T_e/T$, T_e is the electron temperature and T is the mean plasma temperature. Given are the mean value for each element and its standard deviation for the entire set of 12 values of $\beta \in [0.001, 1]$ (see Section 4.2).

4.2 CSW model spectral results

In all the spectral fits, we explored a range of values for the partial heating of the electrons at the shock fronts: $\beta = [0.001, 0.05, 0.1, 0.2, 0.3, 0.4, 0.5, 0.6, 0.7, 0.8, 0.9, 1]$; $\beta = T_e/T$, T_e is the electron temperature and T is the mean plasma temperature ($\beta < 1 \rightarrow 2$ -T plasma, different electron and ion temperatures; $\beta = 1 \rightarrow 1$ -T plasma, equal ion and electron temperatures).

We considered two components of the X-ray absorption: (a) due to the interstellar matter (ISM); (b) due to the stellar wind(s) in WR 140. For the ISM absorption component (kept fixed in the fits), we adopted a value of the foreground column density corresponding to the optical extinction $A_V = 2.50$ mag ($A_V = A_V/1.11$ and table 28 in [van der Hucht 2001](#)) and the [Gorenstein \(1975\)](#) conversion $N_H = 2.22 \times 10^{21} A_V \text{ cm}^{-2}$. The stellar wind absorption shared the same abundances that were adopted for the X-ray emitting plasma in the CSW region.

We note that the chemical abundances of the shocked O-star wind were solar ([Anders & Grevesse 1989](#)). For the shocked WR-star wind, we explored two values for the carbon abundance of C/He = 0.1 and 0.4 by number (bracketing the possible range as deduced from observations of WC stars, see [Eenens & Williams 1992](#), [Dessart et al. 2000](#) also including the value typically adopted in the theoretical models of optical spectra of WC stars, e.g. see table 2 in [Sander et al. 2012](#)), while the other elements had their values typical for the WC stars (by number) as from [van der Hucht et al. \(1986\)](#): H = 0.0, He = 1.0, C = 0.1 (0.4), N = 0.0, O = 0.194, Ne = 1.86×10^{-2} , Mg = 2.72×10^{-3} , Si = 6.84×10^{-4} , S = 1.52×10^{-4} , Ar = 2×10^{-5} , Ca = 2×10^{-5} , Fe = 3.82×10^{-4} . Ar and Ca are not present in the [van der Hucht et al. \(1986\)](#) abundance set, so, we adopted for each of them a fiducial value of 2×10^{-5} . It is worth mentioning that the contribution of the shocked O-star wind to the total observed X-ray emission (flux) of WR 140 is not higher than 5-6%. So, the Ne, Mg, Si, S, Ar, Ca, Fe abundances of the shocked WR plasma were allowed to vary to improve the quality of the fits. Because chemical abundances are not well constrained from undispersed X-ray spectra, we went through the following steps.

1) For each value of parameter β , the X-ray spectra with best photon statistics (*Chandra*-MEG, re-binned to have a minimum of 20 counts per bin) were fitted simultaneously to estimate the abundances. The *xspec* model *gsmooth* was adopted for the line broadening to minimize the amount of CPU time. So, in *xspec* terms the fitted two-absorption model reads: $Spec = wabs(ISM) * wabs(wind) * gsmooth(csw)$, where *csw* is our CSW model with line-broadening

switched off. As seen from Table 2, there is no big scatter between the abundance values for a specific chemical element. We note that the quality of the fits was good in a formal statistical sense for all the values of parameter β : for $\beta \in [0.001, 1] \rightarrow \chi^2 \in [4636, 4938]$ (C/He = 0.1) and $\chi^2 \in [4525, 4952]$ (C/He = 0.4) with 5070 degrees of freedom (dof).

2) The derived abundances for each β were used (kept fixed) in the fits of the *RXTE* spectra adopting the same model as in the first step but with no line broadening (no *gsmooth* component). In these fits, free parameters were the X-ray absorption and the normalization parameter *norm*.

X-ray absorption is found to vary over the binary orbit. And, we note that the most important result from these fits is that a considerable decrease is found for the *norm* parameter at orbital phases near periastron. This is indicative of changing amount of emission measure over the binary orbit. We recall that the emission measure (EM) in the CSW region that results from interaction of spherically-symmetric stellar winds is proportional to the square of the stellar wind mass loss (\dot{M}) and is reversely proportional to the binary separation: $EM \propto n^2 V$, n is the number density, V is the volume; $n \propto \dot{M}/a^2$ and $V \propto a^3$, therefore $EM \propto \dot{M}^2/a$. Since the $1/a$ -dependence of emission measure on the binary separation is accounted for in the hydrodynamic simulations, the fit results are thus suggestive that mass loss varies over the binary orbit. A closer look at derived values of the *norm* parameter near periastron (e.g., bottom panels in Fig. 4) reveals that EM decreases gradually when approaching periastron (phase = 0, i.e. phase = 1) but it does not increase after that. Instead, it levels off and starts increasing only after the orbital phase the WR stellar component is in front.

We thus propose to represent the total variation of EM (the *norm* parameter) by two terms. The first one is responsible for the suggestive variation of the mass loss with binary separation, so, it is symmetric with respect to orbital phase = 0 (periastron). The second one is symmetric with respect to the orbital phase the WR star is in front (phase = 0.00319; Section 2). We note that the basic ‘requirement’ imposed on the specific function describing each term is to gradually decrease at the corresponding phase of symmetry and level off at phases far from it. We underline that the choice of functions in mathematical sense is *not* important as long as they have the mentioned behaviour. For the first term, $\dot{M}(a)$, we assume that binary separation (a) is the independent variable. For the second term, $Scl(\alpha)$, we assume that azimuthal angle (α ; Fig. 2) is the independent variable. We recall that the binary separation is in the range $a \in [1 - e, 1 + e]$ (in units of the semi-major axis), where $e = 0.8964$ (Section 2) is the orbital eccentricity. Also, the azimuthal angle is in range $\alpha \in [0, 180]$ degrees due to suggested symmetry, that is the $Scl(\alpha)$ values for α and $\alpha = 360 - \alpha$ are the same. We have to keep in mind that given the binary ephemeris for each orbital phase we know the binary separation and the azimuthal angle, that is there is a unique correspondence between the latter two quantities. We thus write:

$$\begin{aligned} \dot{M}(a) &= \dot{M}_1 + (\dot{M}_2 - \dot{M}_1) \times \left[1 - \left(\frac{1-e}{a} \right)^{s_1} \right]^{s_2} \\ Scl(\alpha) &= \begin{cases} 1 & \text{if } \alpha \geq \alpha_0 \\ b_1 + (1 - b_1) \times \tanh \left[\left(\frac{\alpha}{\alpha_0 - \alpha} \right)^{b_2} \right] & \text{if } \alpha < \alpha_0 \end{cases} \\ norm &= [\dot{M}(a)]^2 \times Scl(\alpha) \end{aligned} \quad (1)$$

where $\dot{M}_1, \dot{M}_2, s_1, s_2, b_1, \alpha_0, b_2$ are free parameters in the fits.

Table 3. Coefficients in eq. 1

	C / He = 0.1	C / He = 0.4
\dot{M}_1	0.243 ± 0.001	0.236 ± 0.001
\dot{M}_2	0.689 ± 0.010	0.677 ± 0.010
s_1	0.667 ± 0.027	0.656 ± 0.026
s_2	1.003 ± 0.015	1.008 ± 0.015
b_1	0.199 ± 0.002	0.200 ± 0.002
b_2	0.644 ± 0.006	0.650 ± 0.007
α_0	177.5 ± 0.739	178.5 ± 0.572

Note. Values of coefficients in eq. 1 derived from the fits to the normalization parameter (*norm*) as obtained from the fits to the *RXTE* spectra of WR 140. Given are the mean value for each coefficient and its standard deviation for the set’ of $\beta < 0.4$ values (see Section 4.2).

For each case (value) of β , we used eq. 1 to fit the normalization parameter values derived from the spectral fits. We found that eq. 1 is a good representation of the changes of this parameter over the orbital period: an example of the corresponding results is shown in Fig. 4. The two terms $\dot{M}(a)$ and $Scl(\alpha)$ derived for the ‘best’ cases of $\beta < 0.4$ (see below) are shown in Fig. 5 and the corresponding coefficients in eq. 1 are given in Table 3.

As described in Section 4.1, the entire spectral fitting procedure is aimed at getting a value of *norm* = 1. So, we made two more general iterations, adopting the reduced mass-loss rates corresponding to the derived values for each term in eq. 1. Namely, we had to re-run the hydrodynamic simulations, derive the corresponding distribution of the physical parameters in the CSW region and re-do the spectral fits. We note that all this resulted not only in values of *norm* ≈ 1 but in a better quality of the spectral fits. As seen from Fig. 6, the basic improvement is due to the reduced mass-loss rates ($\dot{M}(a)$) and the quality of the fits does not get better by considering the effect of the second term ($Scl(\alpha)$) of eq. 1.

Also, it seems conclusive that two-temperature plasma with $\beta < 0.4$ (i.e. partially heated electrons at the shock fronts) is needed in the CSW region of WR 140 to successfully explain the X-ray emission from this massive binary. In general, we could try to define the ‘best value’ of β , that is the one which provides the best match to the observed spectra. But, approaching this in a standard statistical way shows that the goodness of the fit is equal to 1 for all the cases with $\beta < 0.4$, which means that all these fits are equally good. Thus, we do not think that a more definite conclusion could be drawn rather than the one that two-temperature plasma with $\beta < 0.4$ is present in the CSW region of WR 140. An illustration of the CSW spectral fits is shown in Fig. 7.

It is worth noting that one of the basic effects of the partial heating of electrons in shock fronts ($\beta < 1$) is that the electron temperature is lower (not higher) than the local mean plasma temperature. Therefore, the resulting X-ray emission of the shocked plasma will be ‘cooler’ in this case (two-temperature plasma). This explains why the quality of the fits to the *RXTE* spectra of WR 140 improves when the case of two-temperature plasma is considered. Namely, a closer look at the *RXTE* spectra established that some excess in the *X-ray model emission* starts to emerge at high energies when β increases and approaches unity (i.e. for equal ion and electron temperatures).

However, we have to keep in mind that low-resolution spectra (*RXTE*) are lacking some very important details about the gas kinematics of the emitting X-ray plasma. Therefore, modelling the high-resolution X-ray spectra of WR 140 in detail is a natural step to fill this gap.

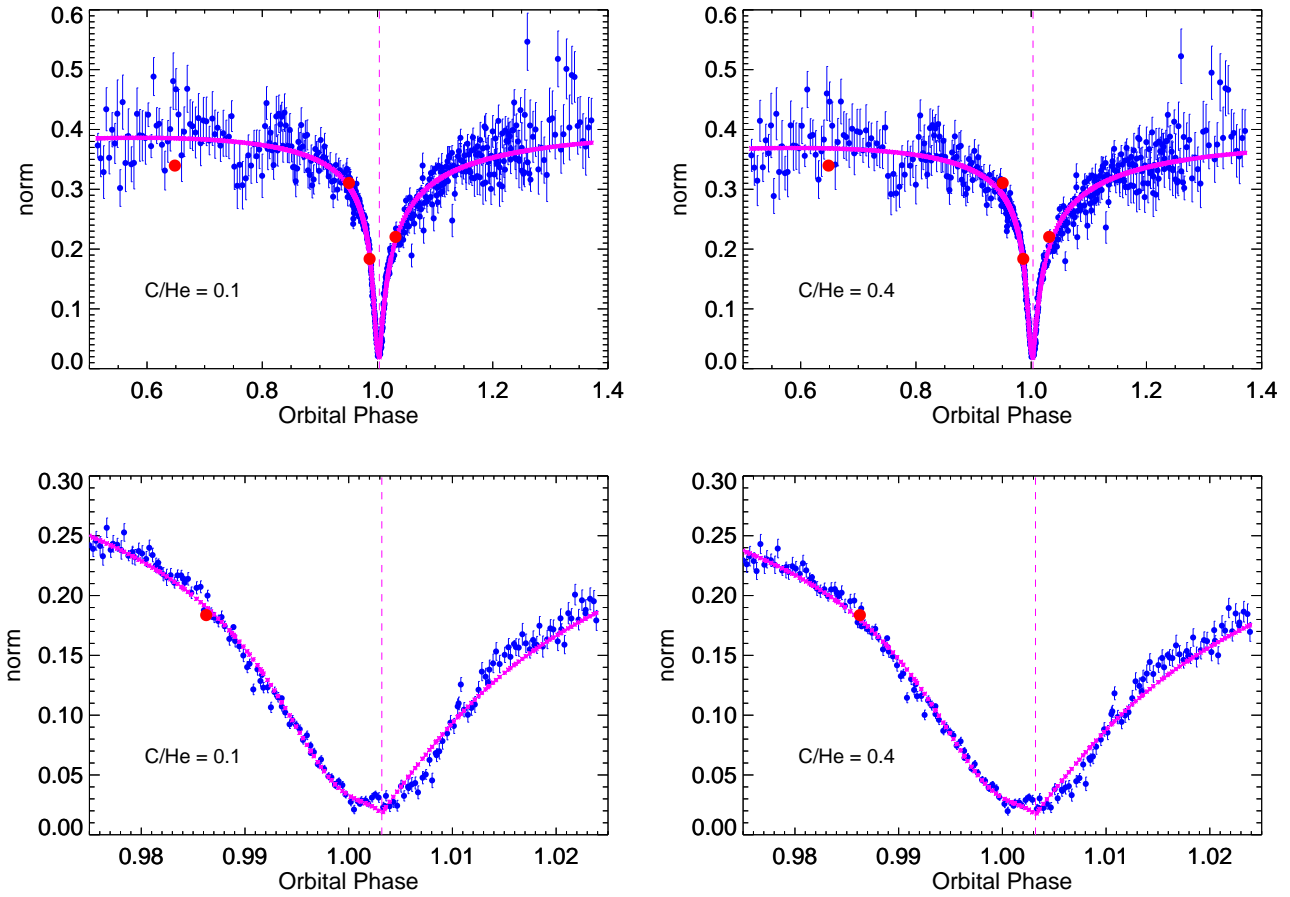


Figure 4. The values of the normalization parameter ($norm$) of the CSW `xSPEC` model as derived from the fit to the *RXTE* (blue dots) and *Chandra* (red filled circles) spectra of WR 140 for the case of different electron and ion temperature ($\beta = 0.1$) and different chemical composition ($C/He = 0.1$; 0.4). The vertical dashed line denotes the orbital phase of WR-star in front. The two-component fit to the normalization parameter (see text for details) is overlaid in magenta colour.

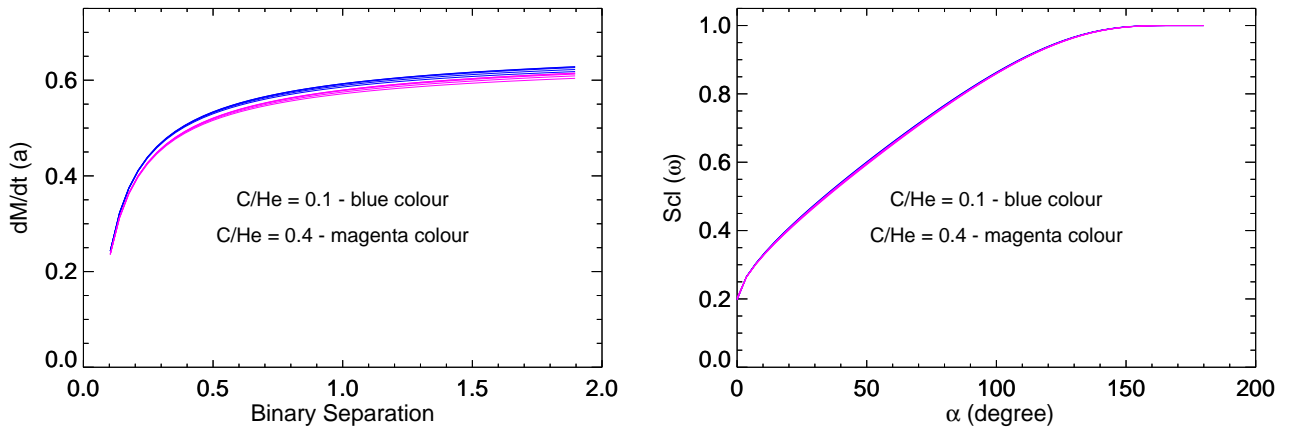


Figure 5. Results from the use of eq. 1 for fitting the values of the normalization parameter ($norm$) over the orbital period for the ‘best’ set of $\beta < 0.4$ values (Section 4.2). The first term $\dot{M}(a)$ and the second term $Scl(\alpha)$ is shown in the left and right panel, respectively. Binary separation is in units of the semi-major axis.

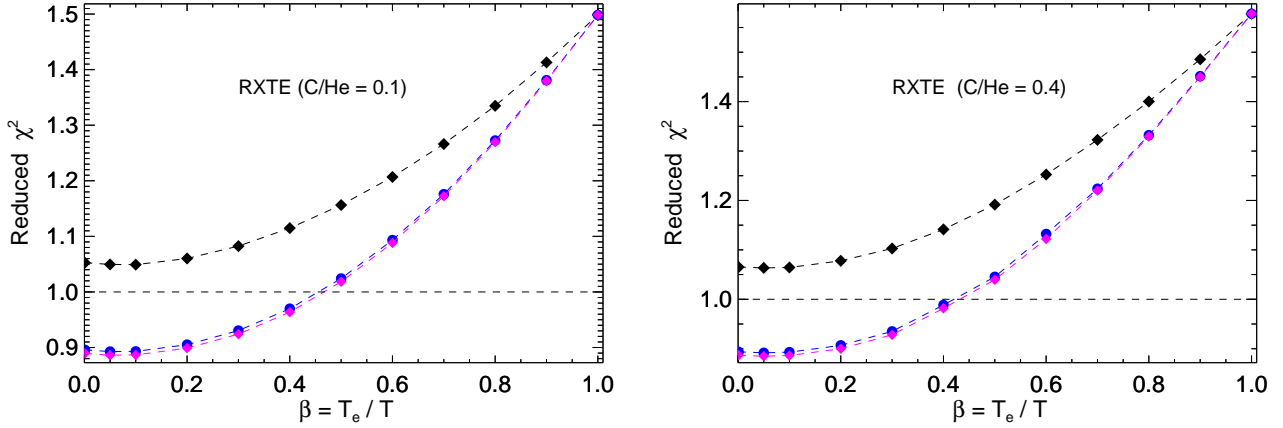


Figure 6. The total reduced χ^2 (dof = 22080) for the entire set of 552 *RXTE* spectra. The top curve (in black) shows the results from the CSW spectral fits with the nominal stellar-wind parameters. The lower two curves presents the results with reduced mass-loss rates as described by terms $\dot{M}(a)$ (in blue colour) and $Scl(\alpha)$ (in magenta colour) of eq. 1, respectively. The χ^2 values are provided in Table A1.

3) Since the gas kinematics of the X-ray emitting plasma is ‘encoded’ in the spectral line profiles, it is therefore important to check whether the CSW model could explain/match the observed line profiles of various ionic species. Similarly to the CSW analysis of the *RXTE* spectra (i.e., correspondingly fixed abundances to those from Table 2), we fitted the high-resolution spectra with spectral model that explicitly calculates the line broadening as derived in the CSW hydrodynamic simulations. As given in Section 4.1, this model also takes into account the stellar wind absorption along the line of sight for each parcel of gas in the CSW region. It also allows for an additional absorption component if the stellar wind absorption is not enough to match the shape of the observed spectrum. This ‘extra’ absorption component has the same abundances as the WR wind. In *xSPEC* terms the fitted model reads: $Spec = wabs(ISM)*wabs(extra)*csw_lines_wind$, where csw_lines_wind is our CSW model with line-broadening and stellar wind absorption along the line of sight taken into account.

For this in-detail check of the CSW picture, we fitted the *Chandra* HEG and MEG spectra adopting one of the ‘best-fit’ CSW models that successfully represent the *RXTE* spectra of WR 140. Namely, we used the CSW model with different electron and ion temperatures for the case of $\beta = 0.1$. Some fit results are shown in Figs. 8 and 9 which illustrate that the CSW model provides line profiles that in general do *not* match well the observed line profiles of the strong line features in the X-ray spectrum of WR 140. We recall that our CSW *xSPEC* model does not take into account the thermal line broadening that may in general have some observational effect, especially, in the case of two-temperature plasma. However, we see that the theoretical line profiles are in general *broader* than those observed. Thus, including additional line broadening would not improve the correspondence between theory and observations.

Another interesting result is that some small (but not zero) ‘extra’ X-ray absorption (i.e., in excess to that of the stellar wind) is needed to match the shape of the observed spectra at least of Obs 1 and Obs 2 (orbital phases 0.9863 and 0.0312, respectively). To explore further this result, we used the same CSW model (but switching off the spectral-line broadening) to fit the *RXTE* spectra of WR 140. Some fit results are shown in Fig. 10. As seen, the fits to the *RXTE* spectra establish that a considerable X-ray absorption in WR 140 is present

at orbital phases near periastron. Most importantly, this absorption is in addition to that from the stellar winds.

It is worth mentioning that signs of X-ray absorption in ‘excess’ to that due to the stellar winds were found also from modelling of undispersed *ASCA* spectra of WR 140 in the framework of the standard CSW picture (see section 4.4.2 in Zhekov & Skinner 2000).

5 DISCUSSION

We carried out a direct modelling of observed X-ray spectra (*RXTE*, *Chandra*) of WR 140 in the framework of the *standard* colliding stellar wind picture in massive WR+O binaries. The good correspondence between the results from the *RXTE* and *Chandra* spectral fits (Figs. 1, 5 and 10) gives us confidence in the derived CSW model results as two of the most important ones are the following. First, a considerable reduction of the emission measure of the X-ray plasma is required at orbital phases near periastron in this binary with high orbital eccentricity to explain its observed X-ray emission. Second, X-ray absorption in excess to that from the stellar winds is present in the massive binary WR 140. On the other hand, a third very important result from modelling the high-resolution spectra (*Chandra*) of WR 140, adopting the *standard* CSW model, is that such a model does not provide a good match to the observed profiles of its strong emission lines (Figs. 8 and 9). We will next discuss their possible implication for the CSW picture in massive binaries.

As shown in Section 4.2, the change of the emission measure can be represented successfully by two terms: one is symmetric with respect to orbital phase = 0 (periastron) and the second term is symmetric with respect to the orbital phase the WR stars is in front (phase = 0.00319): terms $\dot{M}(a)$ and $Scl(\alpha)$, respectively (see eq. 1, Figs. 4 and 5). We recall that the $1/a$ -dependence of the emission measure on the binary separation in a massive binary with eccentric orbit is already taken into account in the hydrodynamic simulations. Therefore, the variation of the emission measure in fact indicates a change of the mass-loss rates. It is generally accepted that the stellar winds of massive stars are not uniform, that is they consist of dense clumps with volume filling factor (clumping) $f < 1$. We could then propose the following interpretation for the change of the emission measure symmetric with respect to periastron (i.e., term $\dot{M}(a)$).

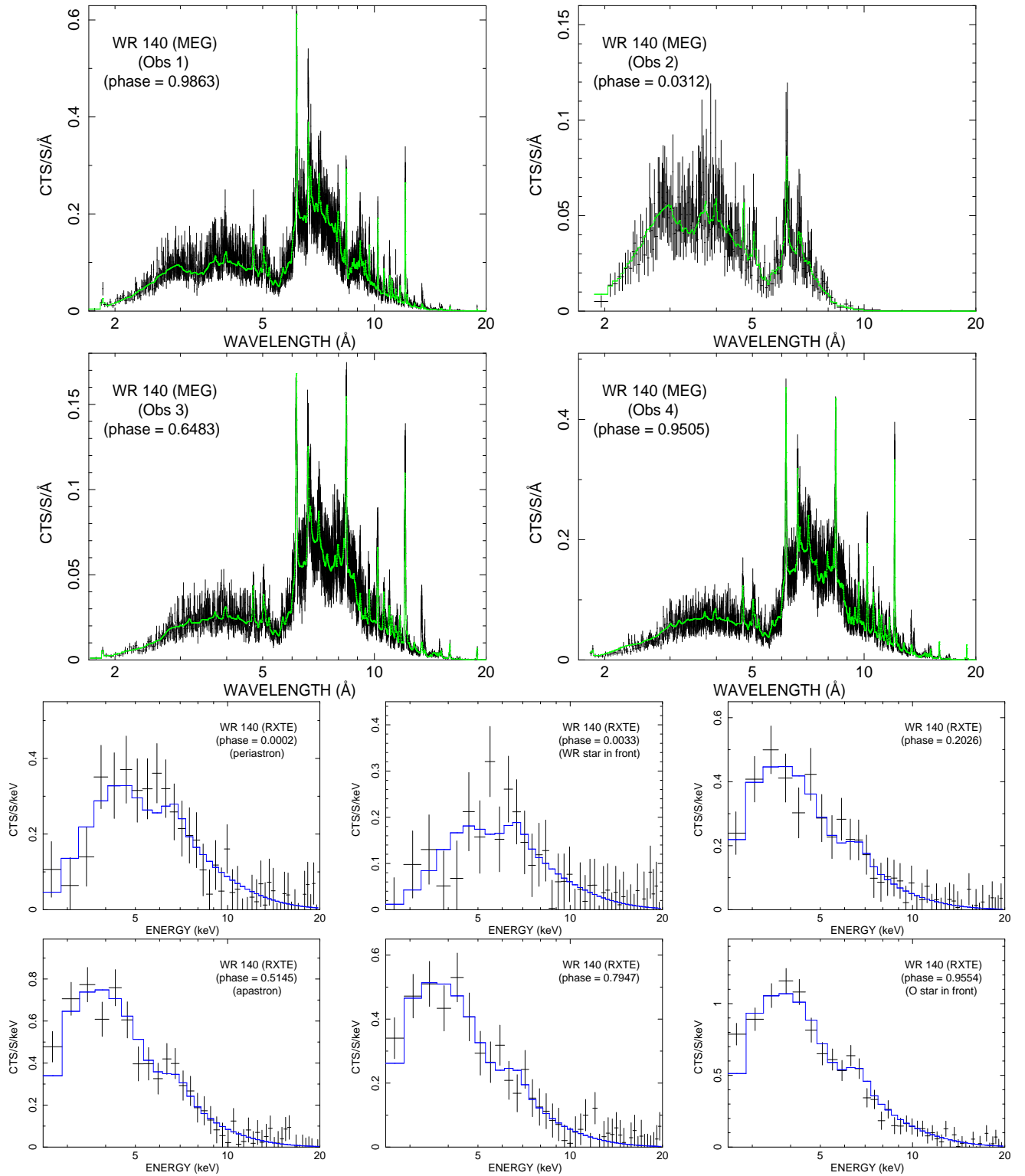


Figure 7. Background-subtracted spectra of WR 140 and the CSW model ($\beta = 0.1$; $C/He = 0.4$) fit. The *Chandra* HETG-MEG spectra were re-binned to have a minimum of 20 counts per bin, while the *RXTE* spectra retained their original binning. A label in each panel provides the value of the orbital phase for the corresponding observation.

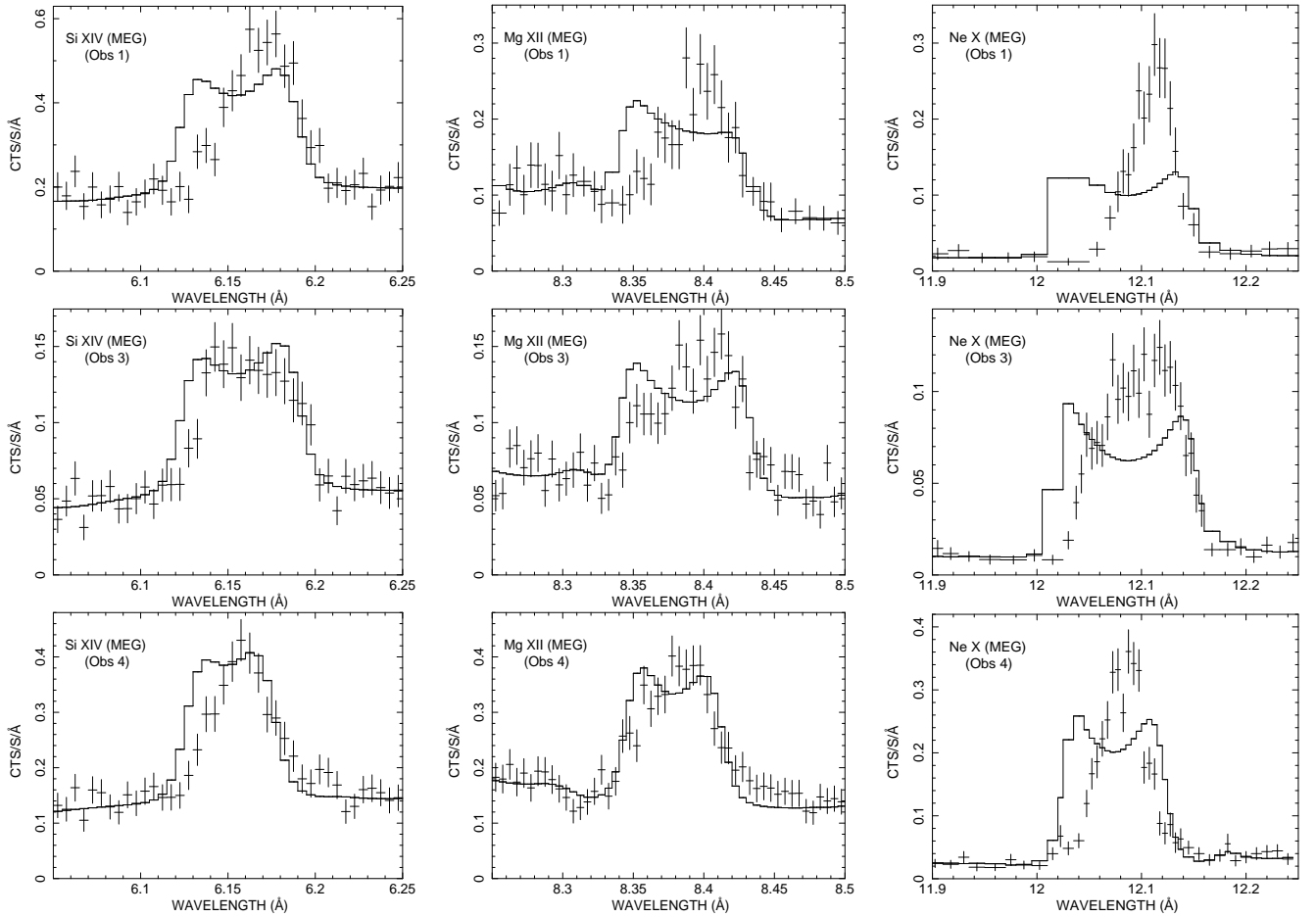


Figure 8. The HETG-MEG background-subtracted spectra of WR 140 and the CSW model ($\beta = 0.1$; $C/He = 0.4$) fit near some strong H-like emission lines (Si XIV 6.18 Å, Mg XII 8.42 Å, Ne X 12.13 Å). The data of Obs 2 are not shown due to the poor photon statistics that provides no valuable pieces of information on the gas kinematics (line profiles).

Namely, the change of the $\dot{M}(a)$ -term over the binary orbit (see Fig. 5) could mean that clumps are dissolved in the CSW region at large binary separations (i.e., near apastron) but are not so at small separations (i.e., near periastron) and can easily cross the interaction region, thus, not contributing to the X-ray emission. The latter is equivalent to smaller *effective* mass-loss rates as deduced from the spectral fits.

Based on numerical hydrodynamic simulations of ‘clumpy’ CSWs in wide binaries, Pittard (2007) concluded that clumps are quickly heated up and dissolved in it after crossing the shock fronts of the CSW zone. In that study, adiabatic CSW zone was considered in a binary system with parameters reminiscent of those in WR 140 at apastron. It is worth mentioning that dissipative processes may also play a role for the physics of CSWs, especially, in wide binaries. As shown by the numerical simulations of Myasnikov & Zhekov (1998), thermal conduction is more efficient at large binary separation all other physical parameters being the same. Therefore, it will facilitate the clumps to heat up and evaporate, i.e. dissolve in the interaction region. Also, we note that the crossing time of the interaction region for a clump is longer at large binary separations (i.e., near apastron) since the width of the interaction region is proportional to the binary separation. As a result, the clump will experience the ‘evaporation force’ for longer time which increases its chances to being dissolved in the interaction region.

As to the $Scl(\alpha)$ -term in the variable emission measure (that symmetric with respect to orbital phase the WR star is in front), we think it could be considered qualitatively in conjunction with results on the ‘extra’ X-ray absorption in WR 140. We note that the latter has its maximum values near the same orbital phase (WR in front) but it is asymmetric with respect to it (see Fig. 10). It may seem speculative, but could it be that all this (the necessity of the $Scl(\alpha)$ -term and the presence of ‘extra’ X-ray absorption) is a hint on *non-spherically-symmetric* stellar wind(s) in the massive binary WR 140?

And, could it be that a similar sign might also be coming from the fact that the *standard* CSW model (i.e. considering interaction of spherically-symmetric stellar winds) failed to produce a good match to the observed line profiles in WR 140 (see Figs. 8 and 9)?

In fact, we ran models with different values of orbital inclination (e.g., $i = 50, 70, 80$ deg; see Section 2) but they did not provide a better match to the observed line profiles. The same is valid for our modelling with increased value of the ram-pressure ratio ($\Lambda = 39$), which in general may produce line profiles with smaller widths. We also tried to mimic a non-spherical absorber (e.g., similar to some disk-like structure as that proposed from radio observations of WR 140; see section 4 in White & Becker 1995) by taking into account *only* the X-ray emission ‘below’ or ‘above’ the orbital plane, or from a certain sector of the CSW cone. However, this toy-play

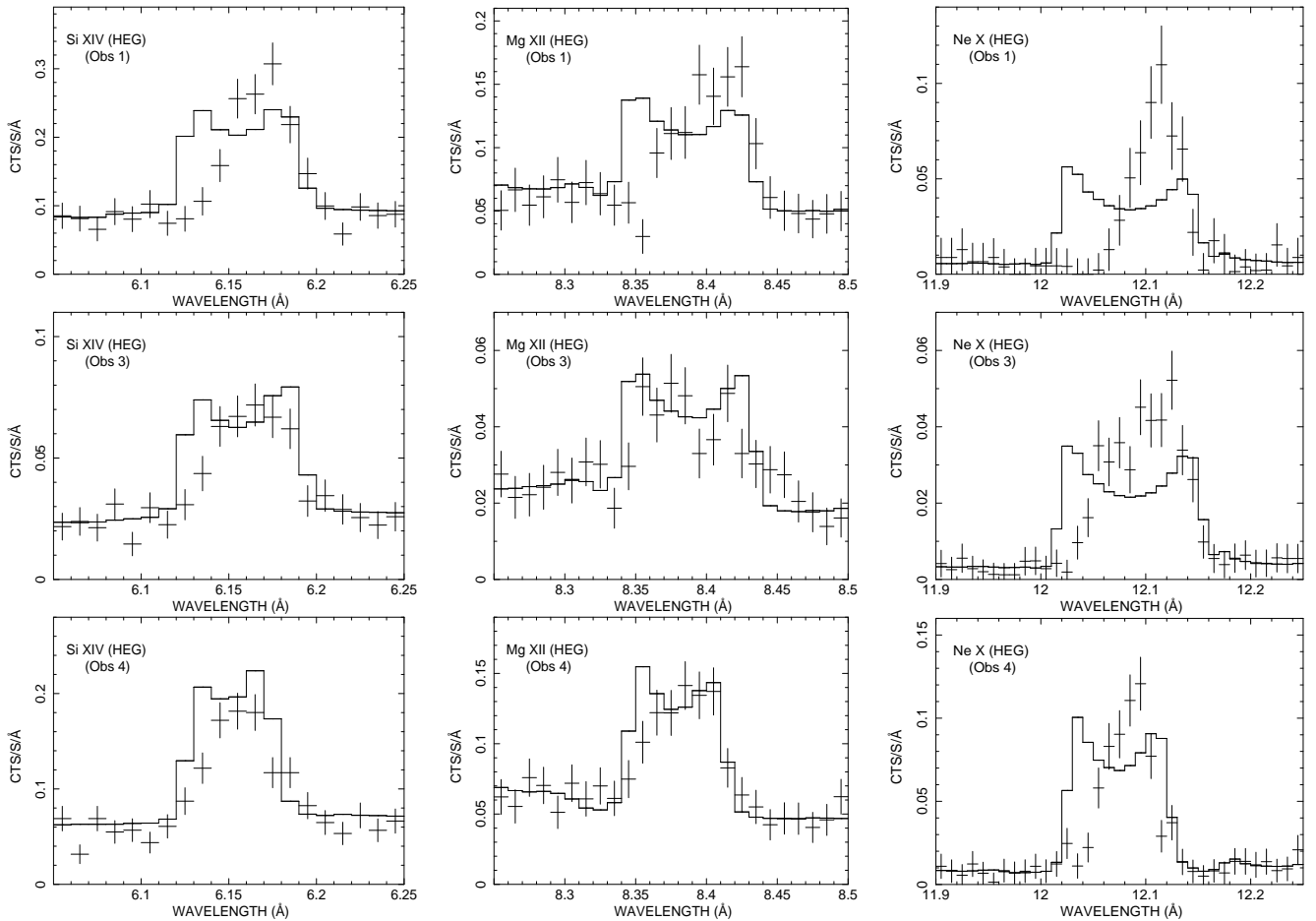


Figure 9. The same as in Fig. 8 but for the HETG-HEG background-subtracted spectra of WR 140 and the same CSW model fit.

modelling did not improve the correspondence between the CSW model line profiles and those observed.

And, we note that the *Chandra* observations Obs 1 and Obs 3 have been carried out at orbital phases that correspond to very similar values of the azimuthal angle: $\alpha = 146$ (Obs 1) and $\alpha = -144$ (Obs 3); note that the case with a given value of α is equivalent to that with the value $\alpha = 360 - \alpha$ and is equivalent to that with the value $-\alpha$; see Fig. 2). This suggests that the resultant line profiles should be almost identical in the case of CSW region produced in collision of two spherically-symmetric stellar winds. However, the observed line profiles (shapes, widths) are quite different between Obs 1 and Obs 3 (e.g., see Figs. 8 and 9).

Thus, it is our understanding that a next step in development of more realistic CSW models could be to consider CSW models with non-spherically-symmetric (e.g., axisymmetric) stellar winds. We have to keep in mind that such a model is definitely a three-dimensional (3D) model. Exploring its parameter space is a heavy task since even if only one of the winds is axisymmetric the resultant interaction region will depend on the orientation in space of the axis of symmetry of the stellar wind that will be changing over the orbit. Nevertheless, it is worth to try, we think.

It is important to mention another feature that adds to complexity of modelling CSWs in massive binaries. As discussed in Zhekov et al. (2020) (see section 4.3 therein), if the winds of massive stars are just ‘clumpy’ (with volume filling factor $f < 1$) it is not clear how clumps manage to collide and form the interaction region in a massive

binary. It is thus reasonable to assume that stellar winds of massive stars are *two-component* flows. The more massive component in the flow consists of dense clumps that may occupy even a very small fraction of the stellar wind volume (e.g., with $f = 0.1 - 0.25$, see Hamann et al. 2019, Sander et al. 2019, and references therein). And, there is a low-density component that fills in the rest of the volume. In such a physical picture, the low-density wind components of both massive stars in the binary interact and set up the ‘seed’ CSW region. The more massive components of the stellar winds (the clumps) then interact with it and provide the strong X-ray emission observed from wide CSW binaries. Note that modelling such a two-component wind interaction will also explicitly require 3D hydrodynamic simulations.

Finally, we recall that the physical picture of two-component stellar winds in massive stars seems to get some support also from the relatively low level of X-ray emission from close WR+O binaries that may likely arise from *adiabatic* CSW shocks of the low-density components of the stellar winds (Zhekov 2012).

6 CONCLUSIONS

The basic results and conclusions from our modelling of the *Chandra* and *RXTE* X-ray spectra of the massive binary WR 140 in the framework of the standard colliding stellar wind picture are as follows.

(i) CSW model spectra match well the shape of the observed X-ray spectrum of WR 140. Models with partial electron heating

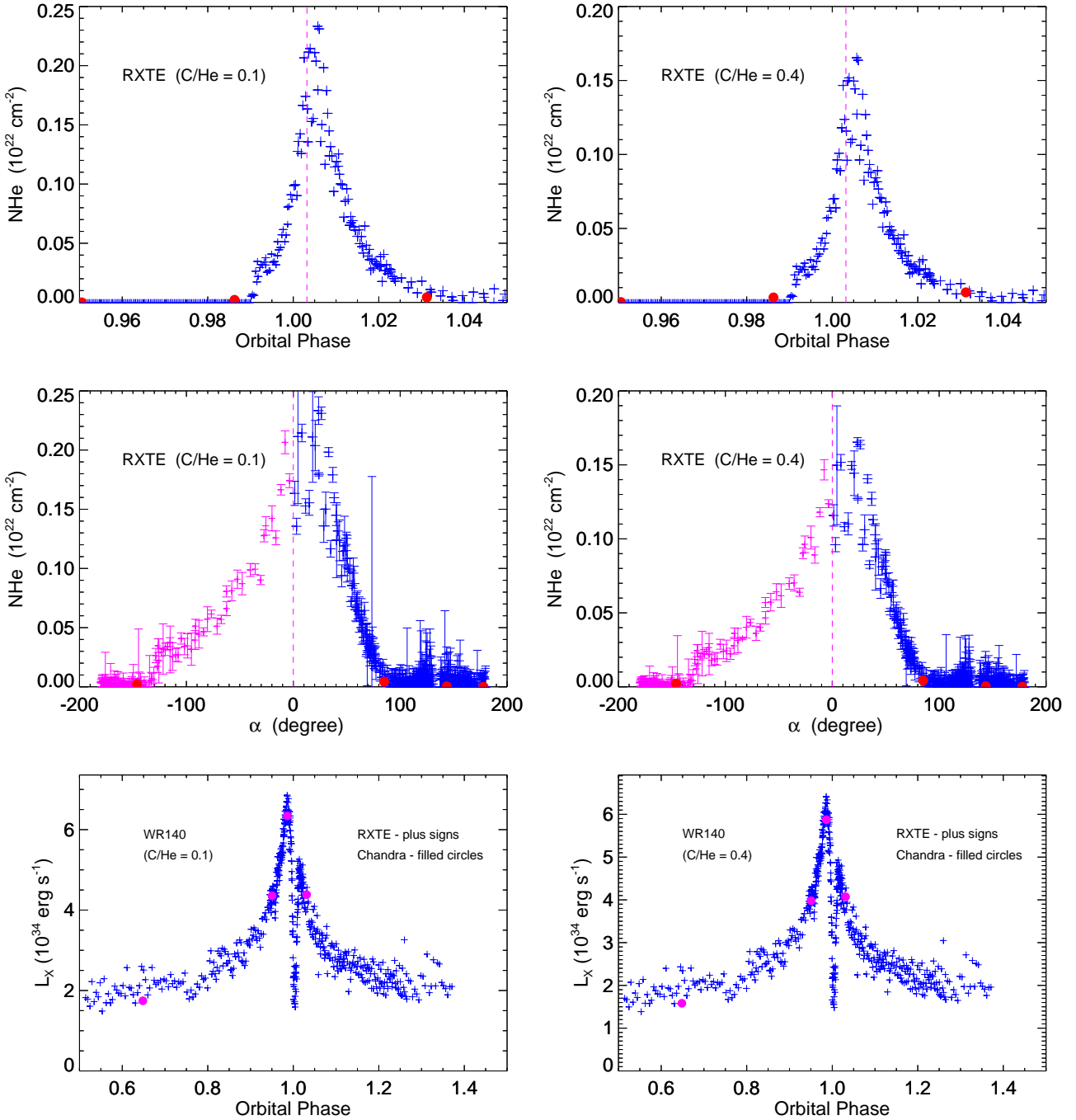


Figure 10. The values of the column density of the ‘extra’ X-ray absorption (i.e., in excess to that of the stellar winds) and the X-ray luminosity (0.5 - 10 keV) as derived from the fit of the CSW model to the *RXTE* (blue plus signs) and *Chandra* (red filled circles) spectra of WR 140 for the case of different electron and ion temperature ($\beta = 0.1$) and different chemical composition ($C/He = 0.1; 0.4$). The top panels show the X-ray absorption at orbital phases near periastron (no error bars plotted for clarity). The middle panels show the X-ray absorption as a function of azimuthal angle α (see Fig. 2). Negative values of α simply denote orbital phases between O-star in front and WR-star in front (see Fig. 2). The vertical dashed line denotes the orbital phase of WR-star in front.

at the shock fronts (different electron and ion temperatures) with $\beta = T_e/T < 0.4$ (T_e is the electron temperature and T is the mean plasma temperature) are a better representation of the X-ray data than those with complete temperature equalization.

(ii) A considerable decrease is found for the emission measure of the X-ray plasma in the CSW region at orbital phases near periastron.

This is equivalent to variable effective mass-loss rates over the binary orbit.

(iii) A considerable X-ray absorption in WR 140 is present at orbital phases near periastron, as this absorption is in excess to that from the stellar winds.

(iv) Fits to the high-resolution spectra showed that the *standard*

CSW model provides line profiles that in general do *not* match well the observed line profiles of the strong line features in the X-ray spectrum of WR 140.

(v) To explain these findings, we propose a qualitative picture for wide massive binaries whose orbits have high eccentricity as is the case of WR 140. In this picture, stellar winds are ‘clumpy’. Due to some dissipative processes (e.g., thermal conduction), clumps are easily dissolved in the CSW region at large binary separations (i.e., near apastron) but are not so at small separations (i.e., near periastron) and can easily cross the interaction region, thus, not contributing to the X-ray emission. The latter is equivalent to variable (e.g., smaller near periastron) *effective* mass-loss rates over the binary orbit. On the other hand, we think that *future* developing of CSW models with *non-spherically-asymmetric* stellar winds might be the way to resolve the mismatch between the theoretical and observed X-ray line profiles and explain the excess X-ray absorption near periastron in WR 140, the *prototype* of CSW massive binaries.

ACKNOWLEDGEMENTS

The author, Svetozar Zhekov, dedicates this study to his dear friend and colleague Artyom Myasnikov. This research has made use of data and/or software provided by the High Energy Astrophysics Science Archive Research Center (HEASARC), which is a service of the Astrophysics Science Division at NASA/GSFC and the High Energy Astrophysics Division of the Smithsonian Astrophysical Observatory. This research has made use of the NASA’s Astrophysics Data System, and the SIMBAD astronomical data base, operated by CDS at Strasbourg, France. The author acknowledges financial support from Bulgarian National Science Fund grant DH 08 12. The author thanks an anonymous referee for valuable comments and suggestions.

DATA AVAILABILITY

The X-ray data underlying this research are *public* and can be accessed as follows. The *Chandra* data sets can be downloaded from the *Chandra* X-ray observatory data archive <https://cxc.harvard.edu/cda/> by typing in the target name (WR 140) in the general search form <https://cda.harvard.edu/chaser/>. The *RXTE* data sets can be downloaded from the *RXTE* observatory part of the NASA’s High Energy Astrophysics Science Archive <https://heasarc.gsfc.nasa.gov/docs/archive.html> by typing in the object name (WR 140) in the general search form <https://heasarc.gsfc.nasa.gov/cgi-bin/W3Browse/w3browse.pl>. Some details on the data reduction are given in Section 3.

REFERENCES

- Anders E., Grevesse N., 1989, *Geochimica Cosmochimica Acta*, **53**, 197
 Arnaud K. A., 1996, in Jacoby G. H., Barnes J., eds, *Astronomical Society of the Pacific Conference Series Vol. 101, Astronomical Data Analysis Software and Systems*. p. 17
 Bailer-Jones C. A. L., Rybizki J., Foesneau M., Mantelet G., Andrae R., 2018, *AJ*, **156**, 58
 Cherepashchuk A. M., 1976, *Soviet Astronomy Letters*, **2**, 138
 Dessart L., Crowther P. A., Hillier D. J., Willis A. J., Morris P. W., van der Hucht K. A., 2000, *MNRAS*, **315**, 407
 Eenens P. R. J., Williams P. M., 1992, *MNRAS*, **255**, 227
 Fahed R., et al., 2011, *MNRAS*, **418**, 2
 Gorenstein P., 1975, *ApJ*, **198**, 95

- Hamann W. R., et al., 2019, *A&A*, **625**, A57
 Lebedev M. G., Myasnikov A. V., 1990, *Fluid Dynamics*, **25**
 Luo D., McCray R., Mac Low M.-M., 1990, *ApJ*, **362**, 267
 Marchenko S. V., et al., 2003, *ApJ*, **596**, 1295
 Monnier J. D., et al., 2011, *ApJ*, **742**, L1
 Myasnikov A. V., Zhekov S. A., 1993, *MNRAS*, **260**, 221
 Myasnikov A. V., Zhekov S. A., 1998, *MNRAS*, **300**, 686
 Pittard J. M., 2007, *ApJ*, **660**, L141
 Pollock A. M. T., 1987, *ApJ*, **320**, 283
 Pollock A. M. T., 2012, in Drissen L., Robert C., St-Louis N., Moffat A. F. J., eds, *Astronomical Society of the Pacific Conference Series Vol. 465, Proceedings of a Scientific Meeting in Honor of Anthony F. J. Moffat*, *Astronomical Society of the Pacific, San Francisco*. p. 308
 Pollock A. M. T., Corcoran M. F., Stevens I. R., Williams P. M., 2005, *ApJ*, **629**, 482
 Prilutskii O. F., Usov V. V., 1976, *Soviet Ast.*, **20**, 2
 Rate G., Crowther P. A., 2020, *MNRAS*, **493**, 1512
 Rauw G., Nazé Y., 2016, *Advances in Space Research*, **58**, 761
 Russell C. M. P., Corcoran M. F., Okazaki A. T., Madura T. I., Owocki S. P., 2011, *Bulletin de la Societe Royale des Sciences de Liege*, **80**, 719
 Sander A., Hamann W.-R., Todt H., 2012, *A&A*, **540**, A144
 Sander A. A. C., Hamann W. R., Todt H., Hainich R., Shenar T., Ramachandran V., Oskinova L. M., 2019, *A&A*, **621**, A92
 Stevens I. R., Blondin J. M., Pollock A. M. T., 1992, *ApJ*, **386**, 265
 van der Hucht K. A., 2001, *New Astron. Rev.*, **45**, 135
 van der Hucht K. A., Cassinelli J. P., Williams P. M., 1986, *A&A*, **168**, 111
 White R. L., Becker R. H., 1995, *ApJ*, **451**, 352
 Williams P. M., 1995, in van der Hucht K. A., Williams P. M., eds, *Proc. IAU Symposium Vol. 163, Wolf-Rayet Stars: Binaries; Colliding Winds; Evolution*, Kluwer, Dordrecht. p. 335
 Williams P. M., 2008, in Benaglia P., Bosch G. L., C.A. C., eds, *Revista Mexicana de Astronomia y Astrofisica Conference Series Vol. 33, Proc. Conf. Massive Stars: Fundamental Parameters and Circumstellar Interactions*. p. 71
 Williams P. M., van der Hucht K. A., Pollock A. M. T., Florkowski D. R., van der Woerd H., Wamsteker W. M., 1990, *MNRAS*, **243**, 662
 Zhekov S. A., 2007, *MNRAS*, **382**, 886
 Zhekov S. A., 2012, *MNRAS*, **422**, 1332
 Zhekov S. A., 2017, *MNRAS*, **472**, 4374
 Zhekov S. A., Park S., 2010, *ApJ*, **721**, 518
 Zhekov S. A., Skinner S. L., 2000, *ApJ*, **538**, 808
 Zhekov S. A., Petrov B. V., Tomov T. V., Pessev P., 2020, *MNRAS*, **494**, 4525

APPENDIX A: SOME RESULTS FROM THE CSW MODEL FITS TO THE RXTE SPECTRA

In Table A1, we provide in detail the reduced χ^2 values for the CSW model fits to the *RXTE* spectra that could be used in supplementary analysis.

This paper has been typeset from a $\text{\TeX}/\text{\LaTeX}$ file prepared by the author.

Table A1. Reduced χ^2 values for the fits to the *RXTE* spectra

β	C / He = 0.1			C / He = 0.4		
	nominal	$\dot{M}(a)$	$Scl(\alpha)$	nominal	$\dot{M}(a)$	$Scl(\alpha)$
0.001	1.052566	0.895815	0.889423	1.065246	0.893618	0.886700
0.05	1.049501	0.892688	0.886263	1.063540	0.891672	0.884810
0.1	1.049102	0.893042	0.886711	1.064347	0.892993	0.886250
0.2	1.060226	0.905153	0.898958	1.077858	0.906784	0.899959
0.3	1.082457	0.930499	0.924067	1.102827	0.935067	0.928148
0.4	1.114851	0.969903	0.963671	1.141406	0.988448	0.981739
0.5	1.156347	1.024172	1.018375	1.191568	1.045426	1.039512
0.6	1.206856	1.093312	1.088236	1.252401	1.132138	1.122070
0.7	1.266157	1.175927	1.172277	1.322603	1.223760	1.219941
0.8	1.334866	1.272470	1.269603	1.400209	1.332027	1.329423
0.9	1.413030	1.380978	1.379454	1.485615	1.451425	1.449769
1.0	1.498292	1.498346	1.498398	1.577701	1.577820	1.577928

Note. The total reduced χ^2 (dof = 22080) for the entire set of 552 *RXTE* spectra for each value of parameter $\beta = T_e/T$ (T_e is the electron temperature and T is the mean plasma temperature) and both basic sets of abundances considered in this study (C / He = 0.1; C / He = 0.4, see Section 4.2). Columns ‘nominal’, $\dot{M}(a)$ and $Scl(\alpha)$ present results from the CSW model fits for the cases with the nominal stellar-wind parameters, reduced mass-loss rates as described by terms $\dot{M}(a)$ and $Scl(\alpha)$, respectively (see eq. 1 and the details in Section 4.2). These results are shown in Fig. 6.